

Ultrastrong coupling circuit QED in the radio-frequency regime

T. Jaako,^{1,*} J. J. García-Ripoll,² and P. Rabl¹

¹*Vienna Center for Quantum Science and Technology, Atominstitut, TU Wien, 1040 Vienna, Austria*

²*Instituto de Física Fundamental, IFF-CSIC, Calle Serrano 113b, Madrid E-28006, Spain*

(Dated: February 28, 2020)

We study a circuit QED setup where multiple superconducting qubits are ultrastrongly coupled to a single radio-frequency resonator. In this extreme parameter regime of cavity QED the dynamics of the electromagnetic mode is very slow compared to all other relevant timescales and can be described as an effective particle moving in an adiabatic energy landscape defined by the qubits. The focus of this work is placed on settings with two or multiple qubits, where different types of symmetry-breaking transitions in the ground- and excited-state potentials can occur. Specifically, we show how the change in the level structure and the wave packet dynamics associated with these transition points can be probed via conventional excitation spectra and Ramsey measurements performed at GHz frequencies. More generally, this analysis demonstrates that state-of-the-art circuit QED systems can be used to access a whole range of particle-like quantum mechanical phenomena beyond the usual paradigm of coupled qubits and oscillators.

I. INTRODUCTION

Circuit quantum electrodynamics (QED) is a rapidly developing field where fundamental processes of quantum light-matter interactions are studied with superconducting qubits (‘artificial atoms’) coupled to microwave resonators and transmission lines [1–3]. Due to the extraordinary combination of strong coupling and very low losses, many quantum optical phenomena, such as vacuum Rabi splittings [2], photon blockade [4, 5] or super- and subradiant decay [6], have already been demonstrated in these systems with very high precision. Moreover, by using high-impedance resonators or by employing galvanic instead of electric coupling schemes, circuit QED systems can overcome fundamental bounds on the coupling strength in conventional cavity QED systems [7, 8]. It is then possible to access so-called ultrastrong (USC) or deep-strong coupling regimes [9–12], where the qubit-photon coupling is comparable to the photon energy and light-matter interactions become non-perturbative. These conditions have recently been demonstrated in experiments with superconducting qubits coupled to microwave resonators and transmission lines [13–18]. When extended to multiple qubits, this regime could enable new applications such as protected quantum memories [19], ultrafast gate operations [20] or entanglement harvesting schemes [21, 22].

In regular cavity- and circuit QED systems with weak or moderate coupling, light-matter interactions are only effective close to resonance, where energy-conserving transitions between photons and atomic excitations can take place. This constraint does no longer apply in the USC regime, where photons and qubits with very dissimilar frequencies can still strongly influence each other. One specific limit of interest in this context is the low-mode-frequency or adiabatic regime [23–27], where the

bare oscillation frequency of the resonator mode, ω_r , is much smaller than the qubit transition frequency, ω_q . In this regime, the qubit state adjusts instantaneously to the slowly varying field amplitude and provides in turn an effective adiabatic potential for the photon mode. This separation of timescales is similar to the Born-Oppenheimer (BO) approximation in the description of nucleus-electron systems in molecular physics [28]. In the weak-coupling limit, this physics finds applications, for example, for the readout of superconducting qubits or quantum dots through the off-resonant coupling to a low-frequency mode [29–31]. In the USC regime, this adiabatic picture is frequently employed in quantum optics and solid state physics to discuss symmetry-breaking effects in Rabi-, Dicke- and Jahn-Teller models, where the ground-state potential surface changes from a shape with a single minimum to a double-well or mexican-hat potential [32, 33]. In Refs. [34–38] it has been shown in more detail that even for a single qubit this change in the adiabatic potential reproduces the properties of quantum-, excited-state- or dissipative phase transitions when $\omega_r \rightarrow 0$. However, reaching this regime with circuit QED systems requires electromagnetic modes in the radio-frequency regime where ω_r is only a few or a few tens of MHz. At these frequencies the mode is thermally occupied even at mK temperatures and electronic measurement techniques, which operate efficiently only above ~ 1 GHz, are not readily available. There is, nevertheless, experimental progress towards the quantum control of such modes. For example, active ground state cooling and the readout of individual photon number states of a 170 MHz electromagnetic resonator has recently been demonstrated [39].

In this paper we study the properties of circuit QED systems in the low-mode-frequency regime by considering a generic setup of two or multiple flux qubits coupled to a radio-frequency resonator. We derive an effective description of this system in terms of adiabatic BO potentials for the electromagnetic mode and discuss the characteristics of the resulting potential energy sur-

* tuomas.jaako@tuwien.ac.at

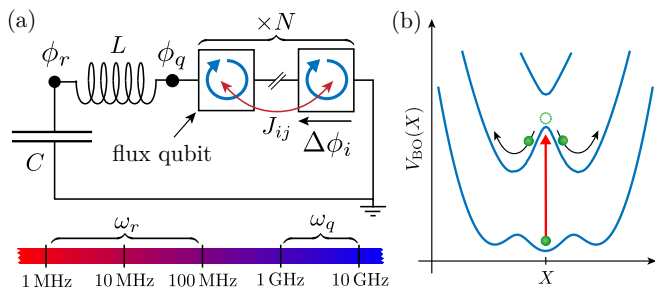


FIG. 1. (a) Setup. Multiple superconducting flux qubits are coupled inductively to a single LC -resonator, giving rise to the collective qubit-photon coupling assumed in Eq. (1). Additional direct qubit-qubit interactions $\sim J_{ij}$ can be engineered through the coupling to auxiliary SQUID loops, as described, for example, in Ref. [42]. (b) In the radio-frequency regime, where the resonator frequency ω_r is much smaller than the qubit frequency, ω_q , the dynamics of the electromagnetic mode can be modelled as an effective particle, which moves along the adiabatic BO potentials generated by the qubits. See text for more details.

faces for different qubit numbers and coupling parameters. Compared to related previous works [23–27, 32, 34–38], our main interest here is in the excited potential curves. These potentials can exhibit multiple first- and second-order symmetry-breaking transitions, even under conditions where the ground state potential still has a single minimum. This leads to a qualitatively new situation where properties of the symmetry-breaking transition occurring at MHz frequencies can be probed via regular qubit-readout techniques operated in the GHz domain. As two specific examples, we describe how the change in the level structure and the dynamics of the wave packet splitting near the transition point can be detected via excitation spectra and Ramsey coherence measurements. This analysis demonstrates that quantum dynamics and phase-transition physics in the radio-frequency regime can be controlled and detected using state-of-the-art superconducting-circuit technology.

The remainder of the paper is structured as follows. After introducing in Sec. II the basic model and its approximate treatment in the low-frequency limit, we provide in Sec. III a general overview of the characteristic features that can appear in the resulting adiabatic potential curves. In Sec. IV and Sec. V we then discuss two schemes for detecting the symmetry-breaking transition in the excited potential. Finally, in Sec. VI we perform a more rigorous justification for the single-mode approximation in a realistic setting and conclude our findings in Sec. VII.

II. CIRCUIT QED IN THE RADIO-FREQUENCY REGIME

We consider a circuit QED setup as shown in Fig. 1, where N flux qubits are coupled inductively to a lumped-element resonator with frequency ω_r and bosonic annihilation (creation) operator a (a^\dagger). By taking only the two energetically lowest states $|g\rangle$ and $|e\rangle$ of each flux qubit into account, the quantized dynamics of this circuit is described by the general cavity QED Hamiltonian [8, 40] ($\hbar = 1$)

$$H_{\text{cQED}} = \omega_r a^\dagger a + \sum_{i=1}^N \frac{\omega_q^i}{2} \sigma_z^i + \sum_{i=1}^N \frac{g_i}{2} (a^\dagger + a) \sigma_x^i + \sum_{i,j=1}^N \left(\frac{g_i g_j}{4\omega_r} + J_{ij} \right) \sigma_x^i \sigma_x^j. \quad (1)$$

Here $\sigma_{x,y,z}$ are the usual Pauli operators and ω_q^i and g_i denote the transition frequency and the coupling strength of each qubit. Apart from the collective qubit-photon coupling in the first line of Eq. (1), this Hamiltonian also contains two direct qubit-qubit interaction terms. The so-called depolarization term $\sim g_i g_j$ represents the gauge-dependent part of the qubit-photon interaction [8, 41] and therefore should not be interpreted as a physical coupling between the qubits. In the current setup its origin can be understood as follows. When expressed in terms of the generalized flux variables indicated in Fig. 1(a), the magnetic energy stored in the inductor reads

$$H_{\text{mag}} = \frac{(\phi_r - \phi_q)^2}{2L}. \quad (2)$$

Here $\phi_r \sim (a + a^\dagger)$ is the oscillator flux variable and $\phi_q = \sum_{i=1}^N \Delta\phi_i$, where the $\Delta\phi_i \sim \sigma_x^i$ represent the flux jumps across each qubit. Therefore, after expanding this energy in terms of the canonical variables, we obtain the photon-qubit interaction together with an apparent all-to-all coupling between the qubits [21, 40].

Equation (1) also includes additional direct qubit-qubit couplings with strengths J_{ij} . Such couplings arise, for example, from the mutual inductance between nearby flux qubits, or, more generally, from a common coupling of the flux qubits to auxiliary superconducting quantum interference devices (SQUIDs), see, for example, Ref. [42]. In the latter case, the range, the sign and the strength of the elements J_{ij} can be fully engineered and controlled by external bias currents. Although the presence of such qubit-qubit couplings is not essential for the main effects described in this work, they provide an additional tuning knob for the resulting potential surfaces discussed below.

A. Extended Dicke model

For concreteness and to simplify the discussion, we will focus in the remainder of our analysis on the case of identical qubits, $\omega_q^i = \omega_q$ and $g_i = g$, and all-to-all inter-qubit interactions, $J_{ij} = J$. In this case, Hamiltonian (1) reduced to the extended Dicke model (EDM) [40, 43]

$$H_{\text{EDM}} = \omega_r a^\dagger a + \omega_q S_z + g(a^\dagger + a)S_x + (1 + \varepsilon)\frac{g^2}{\omega_r}S_x^2, \quad (3)$$

where $S_\alpha = 1/2 \sum_{i=1}^N \sigma_\alpha^i$ are collective spin operators. Here we have adopted the convention $J = \varepsilon g^2 / (4\omega_r)$ [8], such that the dimensionless parameter ε characterizes the relative strength between qubit-qubit and qubit-photon interactions. We emphasize that none of the qualitative findings of this work rely on the assumptions of identical qubits or purely collective couplings. We assume, however, that even in the presence of imperfections the model preserves its parity symmetry, i.e., it remains invariant under the transformation $\sigma_x^i \rightarrow -\sigma_x^i$ and $a \rightarrow -a$. For a more detailed derivation of the EDM for two basic circuit configurations, which correspond to $\varepsilon \geq 0$ and $\varepsilon = -1$, the reader is referred to Refs. [21, 40] and [44], respectively. Further details on the validity of the single-mode approximation assumed in our model are postponed to Sec. VI.

B. Born-Oppenheimer approximation

In regular cavity and circuit QED setups the coupling g between (artificial) atoms and photons is usually small and only resonant processes, where $\omega_r \approx \omega_q$, are relevant. In this regime, the physics of light-matter interactions is most conveniently described in terms of the bare photon number eigenstates, $|n\rangle$, where $a^\dagger a |n\rangle = n |n\rangle$. Close to resonance, these photons can hybridize with matter excitations, which results, for example, in the appearance of a vacuum Rabi-splitting $\sim g\sqrt{N}$ in the excitation spectrum. In this work we are interested in a very different parameter regime, $\omega_r \ll \omega_q, g$ and $g^2/\omega_r \sim \omega_q$. Under such conditions the oscillation of the electromagnetic mode is slow compared to the qubit dynamics, while at the same time the coupling to the qubits has a substantial effect on the cavity and vice versa. Therefore, the representation of the electromagnetic field in terms of the bare photon number states is no longer useful in this regime. Instead, it is more convenient to describe the electromagnetic field as an effective massive particle moving in a set of adiabatic potential surfaces.

To model the static and dynamical properties of the circuit QED system in the limit $\omega_r \rightarrow 0$, we start by introducing the rescaled quadrature variables

$$X = \sqrt{\frac{\omega_r}{2\omega_q}}(a^\dagger + a), \quad P = i\sqrt{\frac{\omega_q}{2\omega_r}}(a^\dagger - a), \quad (4)$$

which correspond to the usual position and momentum operators of a harmonic oscillator. After normalizing all energies with respect to the qubit frequency, i.e., $\tilde{H}_{\text{EDM}} = H_{\text{EDM}}/\omega_q$, we obtain

$$\tilde{H}_{\text{EDM}} = \frac{P^2}{2\mu} + \frac{X^2}{2} + \tilde{H}_q(X), \quad (5)$$

where $\mu = \omega_q^2/\omega_r^2$ is the effective mass and

$$\tilde{H}_q(X) = S_z + \sqrt{2}\lambda X S_x + (1 + \varepsilon)\lambda^2 S_x^2. \quad (6)$$

Here we have defined $\lambda = \sqrt{g^2/(\omega_r\omega_q)}$ as the relevant dimensionless coupling parameter.

The decomposition used in Eq. (5) shows that for $\omega_r \ll \omega_q$ the ‘kinetic’ energy term $\sim P^2$ is small compared to the potential and qubit energies. Thus, in direct analogy to the treatment of nucleus-electron systems in molecular physics, we can apply a BO approximation to separate the fast dynamics of the qubits and the slow motion of the resonator. Under this approximation the eigenstates of the combined system are given by [25, 26]

$$|\psi\rangle_{n,k} = \int dX \phi_{n,k}(X) |X\rangle |\chi_n(X)\rangle, \quad (7)$$

where $|\chi_n(X)\rangle$ is the adiabatic qubit eigenstate. It obeys the Schrödinger equation

$$\tilde{H}_q(X) |\chi_n(X)\rangle = \tilde{E}_n(X) |\chi_n(X)\rangle \quad (8)$$

for a fixed value of X . The dependence of $\tilde{E}_n(X)$ on the position coordinate provides an additional effective potential for the resonator wave function $\phi_{n,k}(X)$, which is a solution of the eigenvalue equation

$$\left[-\frac{1}{2\mu} \frac{\partial^2}{\partial X^2} + \tilde{V}_n(X) \right] \phi_{n,k}(X) = \tilde{\epsilon}_{n,k} \phi_{n,k}(X). \quad (9)$$

Here, $\tilde{V}_n(X) = X^2/2 + \tilde{E}_n(X)$ is the total BO potential associated with the n -th qubit eigenstate. These adiabatic potentials are symmetric around $X = 0$ due to the invariance of Eq. (6) under flipping the signs of X and S_x simultaneously.

The BO approximation neglects couplings between the adiabatic energy eigenstates, which are induced by the momentum operator. The main off-diagonal correction terms, which couple Eq. (9) for different n , are of the form

$$C_{n,m} = \frac{1}{\mu} \frac{\partial \phi_{n,k}}{\partial X} \frac{\langle \chi_m(X) | \sqrt{2}\lambda S_x | \chi_n(X) \rangle}{\tilde{E}_n(X) - \tilde{E}_m(X)}, \quad (10)$$

where we used the relation $\langle \chi_m(X) | \frac{\partial}{\partial X} | \chi_n(X) \rangle = \langle \chi_m(X) | \frac{\partial \tilde{H}_q(X)}{\partial X} | \chi_n(X) \rangle / [\tilde{E}_n(X) - \tilde{E}_m(X)]$. For moderate couplings and electromagnetic eigenstates near the potential minimum, where $\frac{\partial \phi_{n,k}}{\partial X} \sim \sqrt{\mu}$, we obtain a scaling $C_{n,m} \sim \lambda/\sqrt{\mu}$. In all the numerical examples discussed in this work we consider the parameter regime

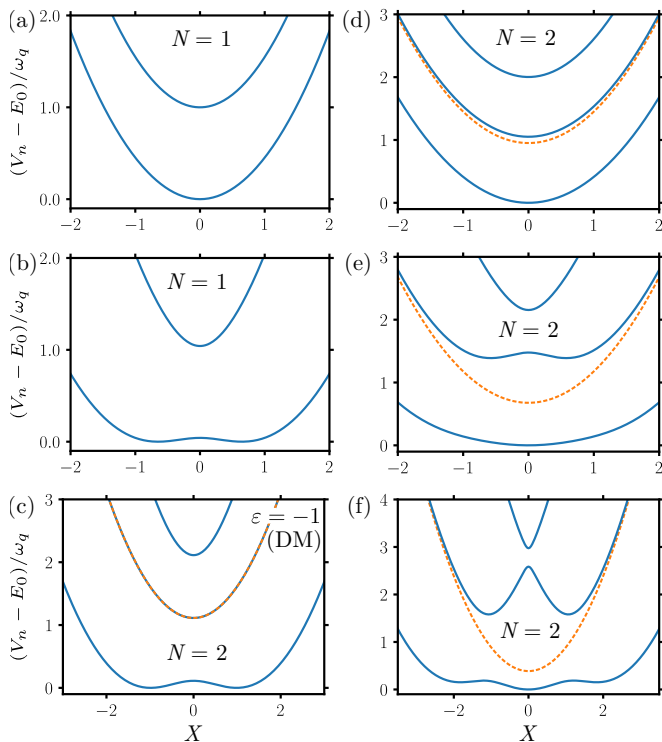


FIG. 2. (a-b) Plot of the BO potentials for the Rabi model ($N = 1$) for a coupling parameter (a) below, $\lambda^2 = 0.1$, and (b) above, $\lambda^2 = 1.5$, the ground-state instability. In (c) the corresponding potentials are shown for the DM [$\varepsilon = -1$ in Eq. (3)] for $N = 2$ qubits and for $\lambda^2 = 0.8$, and in (d-f) for two non-interacting qubits ($\varepsilon = 0$) and (d) $\lambda^2 = 0.1$, (e) $\lambda^2 = 0.8$, and (f) $\lambda^2 = 2.1$. For the cases with $N = 2$ qubits, the solid blue lines represent the triplet states and the dashed orange line the singlet potential. All energies are plotted with respect to the minimum of the lowest potential curve, $E_0 = \min\{V_{n=0}(X)|X\}$.

$\mu = 10^4 - 10^6$, where the adiabatic condition $|C_{n,m}| \ll 1$ is well-satisfied for the relevant potential curves. However, as discussed in Sec. III C below, for large couplings, $\lambda > 1$, some of the excited potential surfaces are only separated by higher-order avoided crossings. In this case, $|E_n(X) - E_m(X)| \ll 1$ and corrections beyond the BO approximation may become relevant.

III. ADIABATIC POTENTIAL SURFACES

The energy landscape formed by all the V_n is fully determined by the qubit Hamiltonian $H_q(X)$ and depends on the interaction parameters λ and ε as well as the number of qubits, N . In this section we summarize the characteristic features of these potentials in different parameter regimes.

A. Ground-state symmetry breaking

In Fig. 2(a) and (b) we first plot $V_{n=0,1}(X)$ for the simplest case of a single qubit, where H_{EDM} reduces to the quantum Rabi model. For $\lambda \ll 1$ the original harmonic potentials $\tilde{V}_{0,1}(X) \simeq X^2/2 \pm 1/2$ are only weakly perturbed and have a single minimum at $X_{\text{min}} = 0$. For increasing coupling strength the ground state potential becomes shallower until it transitions into a double-well potential with two degenerate minima at $X_{\text{min}} \approx \pm \sqrt{\lambda^4 - \lambda_c^4}/(\sqrt{2}\lambda\lambda_c^2)$ above the critical coupling $\lambda_c = 1$. As indicated in Fig. 2(c) for $N = 2$, the same qualitative behavior is also found for the N -qubit Dicke model (DM), which corresponds to the case $\varepsilon = -1$ in the current notation. In this specific situation the potentials have the simple analytic form [25, 32]

$$\tilde{V}_{s,m_z}^{(\text{DM})}(X) = \frac{X^2}{2} + m_z \sqrt{1 + 2\lambda^2 X^2}, \quad (11)$$

and can be labelled by the total spin quantum number s and the spin projection $m_z = -s, s+1, \dots, s-1, s$ associated with the qubit states $|\chi_{s,m_z}(X=0)\rangle$. This result shows that also for larger N the transition occurs first in the ground-state potential, $m_z = -N/2$, but at a reduced coupling parameter $\lambda_c = 1/\sqrt{N}$.

This change from a single-well to a double-well structure of the adiabatic potential is familiar from studies of Rabi-, Dicke- and Jahn-Teller-type models, where even at larger ω_r this picture explains the observed symmetry breaking in the ground state. Here, symmetry breaking means that for $\lambda > \lambda_c$ the tunnel-splitting between the two lowest resonator states, $\Delta\tilde{\epsilon}$, is exponentially suppressed such that in a realistic setting any weak perturbation will randomly localize the system in one of the degenerate minima. Specifically, by approximating the ground-state potential $V_{N/2,-N/2}^{(\text{DM})}(X)$ by an equivalent quartic double-well potential with the same minima and the same barrier height, we obtain (see e.g. Ref. [45])

$$\Delta\tilde{\epsilon}|_{\lambda > \lambda_c} \approx \frac{8}{\sqrt{\pi}} A e^{-S_0}, \quad (12)$$

with an exponent $S_0 = \frac{2}{3} \sqrt{\mu(\lambda^2 - \lambda_c^2)^3(\lambda^2 + \lambda_c^2)}/(\lambda^2 \lambda_c^4)$ and prefactor $A = \sqrt[4]{(\lambda^2 - \lambda_c^2)^5/(\mu(\lambda^2 + \lambda_c^2))}/(\lambda \lambda_c^2)$. This means that for $\lambda \gg \lambda_c$ the tunneling is suppressed by $\Delta\tilde{\epsilon} \sim e^{-2\sqrt{\mu}\lambda^2 N^2/3}$. When passing from the single-well to the double-well configuration the potential becomes purely quartic at $\lambda = \lambda_c$, in which case the minimal energy splitting is [46]

$$\Delta\tilde{\epsilon}|_{\lambda = \lambda_c} = c \sqrt[3]{\frac{\lambda_c^2}{\mu^2}}, \quad (13)$$

with a numerical prefactor of $c \approx 1.1$. This means that the density of states at the transition point, $\tilde{\nu}_{\lambda = \lambda_c} = 1/\Delta\tilde{\epsilon}$, scales as $\sim \sqrt[3]{N\mu^2}$ and diverges in the classical limit $\mu \rightarrow \infty$. Note, however, that when compared to the

density of states of the unperturbed harmonic potential, $\tilde{\nu}_{\lambda=0} = \sqrt{\mu}$, the peak at the transition point is not very pronounced. This illustrates the necessity to use either many qubits or very large ratios $\mu = \omega_q^2/\omega_r^2$ to detect sharp experimental signatures associated with this quasi-divergence. It has been estimated that the regime $\mu > 10^4$ can be reached using effective implementations of the Rabi model in trapped ion systems [47]. In circuit QED, reaching this parameter regime requires resonator frequencies below 100 MHz.

B. Non-interacting qubits

While the DM has been the subject of many theoretical studies, it only represents a very special class of cavity and circuit QED setups with strong ferroelectric interactions [8]. In Fig. 2(d-f) we now show the potential curves for another relevant example of two non-interacting (or only weakly interacting) qubits, where $\varepsilon \simeq 0$. In this case we see that as the coupling parameter λ increases, the absolute minimum of the ground state potential remains at $X_{\min} = 0$, while for $\lambda \gtrsim 1$ two additional local minima appear around $X \approx \pm 2$. More important for the current work, already at an intermediate coupling strength of $\lambda = 1/\sqrt{2}$ a symmetry-breaking transition occurs in the first excited potential, see App. A. As explained in more detail in Secs. IV and V below, this has important practical implications. The symmetry-breaking effect now occurs at an absolute frequency scale set by the qubit frequency $\sim \omega_q$, at which efficient electronic readout techniques are readily available.

Compared to the DM, another qualitative difference is that for $\varepsilon = 0$ (as well as for any $\varepsilon \neq -1$) the degeneracy between potential curves of different spin quantum numbers is lifted by the S_x^2 term. For example, for $N = 2$ we obtain a splitting of (see App. A),

$$\Delta\tilde{E}(X=0) = (1 + \varepsilon)\lambda^2 \quad (14)$$

between the triplet and singlet potentials at $X = 0$. Therefore, even though the oscillator coordinate is zero, there is still an energy penalty for the triplet state compared to the singlet. This somewhat counterintuitive result can be understood by looking at the original magnetic interaction Hamiltonian given in Eq. (2). At $X = 0$, i.e. $\phi_r = 0$, there will be an energy cost for states for which $\phi_q \neq 0$, such as the triplet state. For the singlet this contribution vanishes.

C. General structure

For a larger number of qubits the energy potential landscapes become considerably more involved and depending on λ and ε the individual potentials curves can exhibit various local and global minima. This is illustrated in Fig. 3(a) and (b) for the example of $N = 3$ and

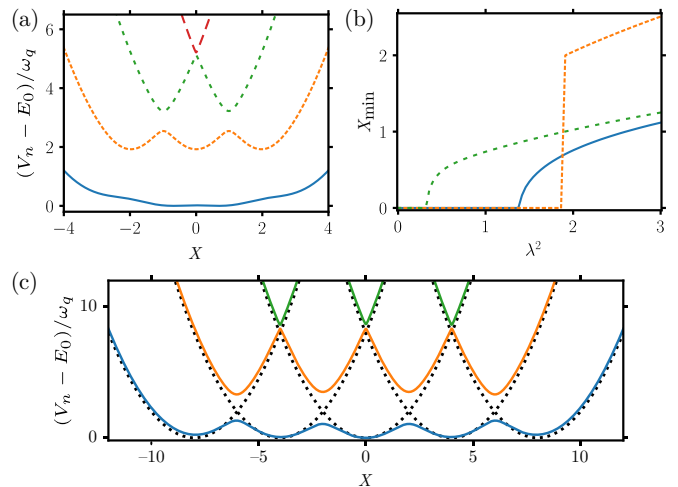


FIG. 3. (a) BO potentials for a system of three qubits and $\varepsilon = 0.02$. At the chosen coupling strength of $\lambda^2 \approx 1.86$, this system exhibits a first-order transition with three degenerate potential wells. (b) Location of the minima of the BO potentials shown in (a) as a function of λ . In this plot we have omitted the highest excited state since its minimum is always located at zero due to symmetry. There is always another degenerate minima located at $-X_{\min}$. (c) Plot of the three lowest BO potentials for a four-qubit system for $\lambda \gg 1$ and $\varepsilon = 0$. The black dotted lines indicate the zeroth-order potentials given in Eq. (15). See also Ref. [40]. Note that for better visibility, all the plots only show the potential curves for qubit states with maximal spin $s = N/2$.

$\varepsilon = 0.02$. Apart from the formation a double-well structure in the ground- and second excited potential curve, in this case we also obtain a triple-well potential with three degenerate minima at a value of $\lambda^2 \simeq 1.86$. This situation corresponds to a first-order phase transition point, where the potential at $X = 0$ remains stable, but the two outer wells become lower in energy after the transition point [cf. Fig. 3(b)].

For a fully symmetric system the total number of distinct potential curves scales as $(N/2 + 1)^2$ (for an even number of qubits) and as 2^N , if different parameters for each qubit are taken into account. To obtain a better intuition about the basic potential landscapes that can arise, it is instructive to consider the limit of very large coupling, $\lambda \gg 1$, following the analysis presented in Ref. [40]. In this limit, the terms $\sim S_x$ and $\sim S_x^2$ dominate over the bare qubit splitting $\sim S_z$. By neglecting the contribution of the S_z term completely, the eigenstates $|\chi_{s,m_x}^0(X)\rangle$ are also eigenstates of S_x and can be labelled by the total spin s and its projection along the x -axis, m_x . The corresponding zeroth-order potential curves are

$$\tilde{V}_{s,m_x}^{(0)}(X) = \frac{1}{2} \left(X + \sqrt{2}\lambda m_x \right)^2 + \varepsilon\lambda^2 m_x^2, \quad (15)$$

which are just a set of displaced parabolas indicated by the dashed lines in Fig. 3(c). As detailed in Ref. [40] and App. A, the presence of the S_z term in the full

model leads to a coupling between the states with m_x and $m_x \pm 1$. Focusing on the limit of very small values for ε , this coupling lowers, first of all, each well by $\Delta\tilde{V}_{s,m_x} = (m_x^2 - s(s+1))/(2\lambda^2)$, due to second-order couplings to energetically higher potentials. Further, at the crossing points $X \simeq -\lambda(2m_x + 1)/\sqrt{2}$, the S_z terms lifts the degeneracy and leads to an avoided crossing with a splitting of $\tilde{\Delta}_{m_x,m_x+1} = \sqrt{s(s+1) - m_x(m_x + 1)}$. As indicated in Fig. 3(c), the actual adiabatic potentials $V_n(X)$ are the resulting connected potential curves. Note that in this picture, which holds for $\lambda \gg 1$, the excited potentials are only separated through higher-order avoided crossings. For general λ , the potential energy surface can then be understood as a smooth interpolation between the stack of parabolas $\tilde{V}_{s,m_z}(X) = m_z + X^2/2$ for the uncoupled system into the degenerate-well structure depicted in Fig. 3(c).

D. Weak-coupling limit

Finally, let us briefly remark on the limit $\lambda \ll 1$, where the system is far away from the instability points. In this case we can expand the adiabatic potential to second order in λ to obtain a state-dependent shift of the oscillation frequency, $\omega_r^{m_z} = \omega_r + m_z\delta\omega_r$ with $\delta\omega_r = g^2/(2\omega_q)$. As long as $\delta\omega_r < \omega_r$, we can make a rotating wave approximation and describe this shift in terms of an effective Hamiltonian

$$H_{\text{eff}} \simeq \omega_r a^\dagger a + \omega_q S_z + \frac{g^2}{4\omega_q} (2a^\dagger a + 1) S_z \quad (16)$$

$$+ \left[(1 + \varepsilon) \frac{g^2}{2\omega_r} - \frac{g^2}{4\omega_q} \right] (\tilde{S}^2 - S_z^2),$$

which corresponds to the usual Stark-shift Hamiltonian for a far detuned cavity QED system. The third term in the first line of Eq. (16) represents a shift of the qubit frequency proportional to the cavity photon number. This type of interaction is frequently encountered in measurement schemes for quantum dots or superconducting qubits [3, 29–31] and has been exploited in Ref. [39] to resolve individual photon number states of a 170 MHz resonator [48]. At slightly larger couplings or even lower resonator frequencies, where $\delta\omega_r \gtrsim \omega_r$, the photon number is no longer a conserved quantity and this picture breaks down.

IV. EXCITATION SPECTRUM

In regular circuit QED systems both ω_r and ω_q are in the GHz regime and both the qubit and the resonator mode can be probed using efficient electronic readout techniques. In the RF domain this is no longer possible using conventional methods and therefore all the properties of the electromagnetic mode must be inferred through measurements performed on the qubits. As a

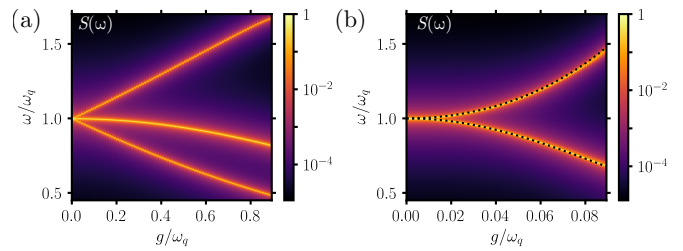


FIG. 4. Spectrum $S(\omega)$ of the EDM for $N = 2$ qubits and (a) on resonance, $\omega_r = \omega_q$, and (b) for $\omega_r/\omega_q = 0.01$. The black dotted lines in (b) indicate the energy of the triplet and singlet potential, relative to the ground state and at $X = 0$. Note that for the parameters assumed in (b) the symmetry-breaking transition occurs at a value of $g/\omega_q \simeq 0.07$. For both plots we have used a fixed decay rate $\Gamma/\omega_q = 0.005$ for all excited qubit states.

first example, we consider in this section the single-qubit excitation spectrum $S(\omega)$, which is proportional to the excited state population of the first qubit when being driven by a weak external field of frequency $\omega \sim \omega_q$. The excitation spectrum is then given by

$$S(\omega) = \frac{\Gamma}{2} \text{Re} \int_0^\infty d\tau \langle \sigma_x^1(\tau) \sigma_x^1(0) \rangle e^{i\omega\tau}, \quad (17)$$

where the expectation value is taken with respect to the equilibrium state of the systems in the absence of the driving field. In Eq. (17) we have introduced a characteristic decay rate Γ , with which the correlation function decays. Since in the parameter regime of interest the qubits are not strongly perturbed by the coupling to the resonator mode, Γ can simply be taken as the bare decay rate of the excited qubit state. In the numerical examples discussed in this section we assume moderate values of $\Gamma \sim \omega_r$, which is still large compared to decoherence rates achieved with state-of-the-art flux qubits [49].

A. Mode splitting in the low-frequency regime

In a first step we assume that the combined system is prepared close to the absolute ground state $|\text{GS}\rangle$ (for example by actively cooling the resonator mode [39]). In this case the excitation spectrum is given by

$$S(\omega) = \sum_f \frac{1}{4} \frac{\Gamma^2 |\langle f | \sigma_x^1 | \text{GS} \rangle|^2}{(\omega - \omega_f)^2 + \Gamma^2/4}, \quad (18)$$

where the sum runs over all final states $\langle f |$, which are separated by a frequency ω_f from the ground state.

In Fig. 4 (a) and (b) we first compare the excitation spectrum of a conventional, i.e., resonant cavity QED system with the case of a circuit QED system in the low-frequency regime. For both plots $N = 2$ and we use the more common convention to plot the spectrum as a function of the coupling strength g instead of λ . In this case

the resonant system exhibits the familiar Rabi splitting $\sim \sqrt{2}g$, which arises from the hybridization of the photon with the triplet state $|T\rangle$. This splitting is visible for $\sqrt{2}g > \Gamma$, which defines the strong coupling regime for a resonant cavity QED system. The additional resonance in the middle is the singlet state $|S\rangle$. The singlet state is decoupled from the cavity mode, but its energy relative to the ground state still decreases for larger coupling strengths.

In the radio-frequency regime, where $\omega_r/\omega_q = 0.01$, the mode frequency is no longer resolved on the scale of this plot. However, the cavity mode has still a drastic influence on the spectrum through the induced splitting between the triplet and the singlet state [see Eq. (14)]. To be observable, this splitting must exceed the qubit decay rate Γ and therefore we identify

$$g > \sqrt{\Gamma\omega_r} \quad (19)$$

as the minimal strong-coupling condition for the low-frequency regime.

B. Probing the symmetry-breaking transition

The dashed lines in Fig. 4(b) indicate the excitation frequencies derived from the energies $V_n(X=0)$. The perfect agreement demonstrates that the dominant peaks of $S(\omega)$ at low temperatures probe the adiabatic potentials curves at $X=0$. This can be understood in terms of the BO wave function in Eq. (7) and the fact that for small and moderate couplings the qubit states $|\chi_n(X)\rangle$ are only weakly dependent on X . The excitation spectrum can then be approximated as

$$S(\omega) \simeq C \sum_k \frac{\Gamma^2 |\langle \phi_{1,k} | \phi_{0,0} \rangle|^2}{(\omega - \omega_{k0})^2 + \Gamma^2/4}, \quad (20)$$

with a constant prefactor $C = |\langle \chi_1(0) | \sigma_x^1 | \chi_0(0) \rangle|^2/4$ and $\omega_{k0} = \epsilon_{1,k} - \epsilon_{0,0}$. We see that the spectrum is mainly determined by excited states with a big overlap with the ground-state wave function $\phi_{0,0}(X)$, which only extends over a scale $\sim 1/\sqrt{\mu}$ around $X=0$. As a result, the spectral lines shown in Fig. 4(b) exhibit no particular feature at the transition point $\lambda^2 = 0.5$, which corresponds to the value of $g/\omega_q \simeq 0.07$ in this plot.

To identify spectral signatures of the symmetry-breaking transition in the excited state, Figs. 5(a) and (b) now show a zoom of the triplet line for $\lambda \geq \lambda_c$ together with the lineshapes of $S(\omega)$ for different values of λ below and above the transition point. For $\lambda < \lambda_c$ we observe a small decrease of the height of the resonance peak, which can be mainly attributed to the decrease in C , i.e., the change in the qubit transition matrix element. However, at $\lambda = \lambda_c$ there is an additional sudden drop in the height of the resonance, which for $\lambda > \lambda_c$ also gets substantially broader. This suppression can again be understood from the overlap between $\phi_{0,0}(X)$ and the few lowest wave

functions in the excited state potential, which become considerably broader at the transition point. For sufficiently small Γ , the appearance of additional sidebands below the main spectral line indicate the excitation of motional states located in one of the two displaced potential wells.

C. Spectrum at finite temperature

As a second approach to observe the structural change in the excited state potential more directly, we consider in Fig. 5(c) the excitation spectrum at finite temperature. In this case, Eq. (20) must be averaged over a thermal distribution of initial states $|\phi_{0,k}\rangle$. This means that also resonator states further away from the center contribute and $S(\omega)$ probes the excited-state potential over a much larger range. For the considered temperature of $k_B T/\omega_q = 0.1$, the qubits are initially still in the ground state with high probability, while a large number of resonator states $\sim k_B T/\omega_r = 10$ are occupied. We see that under such conditions, the triplet line splits into two distinct branches after the transition point. As illustrated in Fig. 5(d), these two lines correspond to the energy separations between the potential curves evaluated at $X=0$ and at the minima $X=X_{\min}$ of the excited state potential, respectively. Since this measurement does not require any pre-cooling of the resonator, it provides a simple way to detect first signatures of the structural change of the potential curve.

V. WAVE PACKET DYNAMICS

In this section we discuss another technique to detect changes in the potential structure through the corresponding change in the wave packet dynamics. For this purpose we consider again a situation where the ground state potential remains stable while the first excited potential curve exhibits a symmetry-breaking transition. The basic idea is to perform a Ramsey-type measurement as depicted in Fig. 6(a). Here the system is initially prepared in a superposition between the ground and the first excited qubit state such that the electromagnetic mode moves along two different potential curves simultaneously. Measurements of the qubit coherence can then be used to determine the overlap between the two wave packets as a function of time.

In Fig. 6 we illustrate this measurement protocol for the same setting as in the previous section, $N=2$ and $\varepsilon=0$. In this case, the symmetry-breaking transition occurs first in the excited potential at $\lambda = 1/\sqrt{2}$. For this parameter, the ground-state potential is still approximately harmonic and active cooling methods can be applied to initialize the system in the absolute ground state $|\Psi(t=0)\rangle = |\text{GS}\rangle \simeq |\phi_{0,0}\rangle \otimes |\chi_0(0)\rangle$. In a first step a microwave field of frequency ω_d is used to implement a $\pi/2$ -rotation, which prepares the qubit state in an

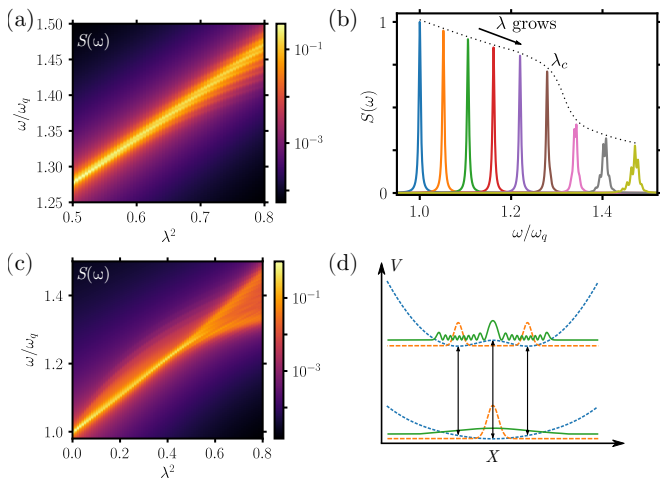


FIG. 5. (a) Zoom of the triplet line of the spectrum $S(\omega)$ shown in Fig. 4 (b) for coupling parameters above the transition point. (b) The resonance peaks of $S(\omega)$ are plotted for couplings $\lambda^2 = 0$ to $\lambda^2 = 0.8$ with steps of 0.1. The black dotted line is a guide to the eye. (c) Plot of the spectrum $S(\omega)$ for a finite temperature of $k_B T/\omega_q = 0.1$. As illustrated in (d), in this case the wider thermal spread of the initial resonator state (lower green solid line) compared to the ground state wave packet (lower orange dashed line) enables transitions into excited states which are localized in the wells, away from $X = 0$. For all plots we have assumed $\mu = 10^4$ and $\Gamma/\omega_q = 0.005$.

equal superposition between $|\chi_0(0)\rangle$ and the triplet state $|\chi_T(0)\rangle$. During this time the system evolves according to the Hamiltonian $H(t) = H_{\text{EDM}} + H_{\Omega}(t)$, where

$$H_{\Omega}(t) = \Omega \cos(\omega_d t + \theta) \sigma_x^1. \quad (21)$$

To prepare the superposition with a fidelity of about 0.95, we set $\theta = 0$, tune the frequency to resonance, $\omega_d = V_T(0) - V_0(0)$ and optimize the pulse time, $\tau_{\pi/2} \sim \pi/(2\Omega)$, for each set of parameters. Next, the system evolves freely for a waiting time τ_w during which the wave packet propagates along two different potential curves. In a last step, a second $\pi/2$ -rotation, now with an optimized phase θ , is applied, such that for $\lambda = 0$ the qubits would be rotated back into the ground state. In the interacting system, variations of the return probability $P_0(\tau_w) = \text{Tr}\{\rho(t_f)|\chi_0(0)\rangle\langle\chi_0(0)|\}$, where $\rho(t_f)$ is the density operator of the system at the final time $t_f = 2\tau_{\pi/2} + \tau_w$, can be used to probe the wave packet dynamics during the free evolution time. This probability can be measured, for example, via regular dispersive readout schemes for qubits [1].

In Fig. 6(b) we plot the return probability P_0 as a function of τ_w and for varying coupling strengths. Note that in the numerical simulations the phase of the second $\pi/2$ -pulse, θ , has been adjusted for each parameter set to compensate trivial phase rotations due to a fixed energy offset between the ground and the excited state. The remaining variations then depend only on the wave

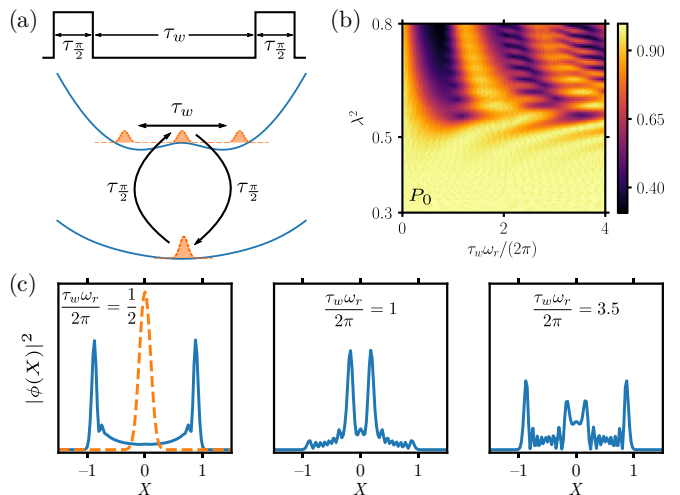


FIG. 6. (a) Illustration of the Ramsey protocol for measuring the wave packet dynamics in the excited state potential. At first the system is prepared in an equal superposition between the ground- and the excited state with different adiabatic potentials. During a waiting time τ_w the resonator wave packets evolve freely in these potentials. After a second $\pi/2$ -pulse, the probability to return to the ground state, $P_0(\tau_w)$, is measured. (b) Plot of the resulting return probability P_0 as a function of the free evolution time and for varying coupling strengths. (c) Snapshots of the resonator wave function for $\lambda^2 = 0.8$. The initial Gaussian wave packet (orange dashed line in the first panel) is a superposition of many eigenfunctions $\phi_{1,k}$ of the double-well potential and quickly starts to spread out and swash back at a later time. Note that for all plots only the coherent dynamics given by H_{EDM} for $\varepsilon = 0$ has been simulated.

packet dynamics and clearly distinguish the regime below and above the transition point. In the former case both potential curves are approximately quadratic and both wave packets remain localized around the origin. Above the transition the part of the wave packet promoted to the excited potential curve is expelled from the central region and undergoes oscillations. The resulting periodic decrease and revival of the wave packet overlap is clearly seen in the Ramsey fringes.

We verify that the observed modulation frequency in the Ramsey signal, which increases with larger λ , is consistent with the dynamics of a wave packet that is initialized at the center of the corresponding double-well potential. This confirms that the described Ramsey-protocol probes the wave packet dynamics in the excited state potential, more precisely, its overlap with the Gaussian ground state at $X = 0$. To further illustrate this point, Fig. 6(c) shows four snapshots of the actual resonator wave function during the protocol, after projecting the system on the excited triplet state $|\chi_T(0)\rangle$. Initially, at $\tau_w = 0$, the wave packet is a Gaussian centered around $X = 0$. After a waiting time $\tau_w \sim \omega_r^{-1}$ most of the wave packet has propagated away from the central region, reducing the overlap with the ground state wave function.

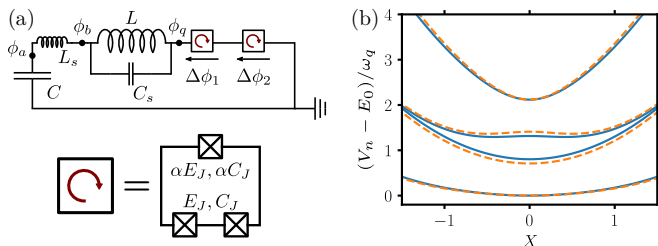


FIG. 7. (a) Sketch of an extended circuit model, which includes the self-capacitance C_s and the self-inductance L_s of the LC -resonator. This can be used to estimate the influence of a higher excited resonator mode with frequency $\omega_{\text{ex}} \approx 1/\sqrt{L_s C_s}$. The qubits are modelled as a superconducting loop intersected by three Josephson junctions, where the size of the upper junction is scaled by a parameter α . (b) Comparison of the BO potentials resulting from the full two-mode circuit shown in (a) (blue solid lines) and the ideal BO potentials from the single-mode EDM (orange dashed lines). The parameters used for this plot are summarized in Table VIB. Note that for the simplified single-mode model the capacitance C_J has been adjusted to have the same qubit frequency ω_q in both simulations ($C_J \simeq 3.5$ fF for single mode circuit).

At even longer times, the reflected wave packets return, but due to the nonlinearity of the potential there is no perfect revival. This explains also the overall decay of the Ramsey fringes over a few oscillation periods. Note that in order to resolve these revivals, the qubit decoherence time T_2 must be longer than $\tau_w \sim \omega_r^{-1}$. Even for a resonator frequency as low as $\omega_r/(2\pi) \approx 10$ MHz, this condition can be fulfilled with realistic coherence times of $T_2 = 1 - 100 \mu\text{s}$ [49].

VI. IMPLEMENTATION

In our model introduced in Sec. II we have considered the coupling of multiple flux qubits to a single resonator mode. For resonant systems, $\omega_r \approx \omega_q$, and moderate couplings such a situation can be realized by using a lumped-element LC resonator. In this case the frequency of the fundamental mode, ω_r , can be well separated from the next higher excitation mode with frequency ω_{ex} , such that even under USC conditions $\omega_{\text{ex}} \gg \omega_r, \omega_q, g$ [16]. However, to observe the physics described in this work, we are interested in rather extreme ratios $\omega_q/\omega_r \gtrsim 100$, where the validity of the single-mode approximation must be evaluated in more detail.

A. Two-mode circuit

Figure 7(a) shows a more realistic model for a two-qubit circuit QED system, where the self-capacitance C_s of the inductor and the self-inductance L_s of the capacitor are taken into account [50]. In this case the

resonator supports a second high-frequency mode with $\omega_{\text{ex}} \sim 1/\sqrt{L_s C_s}$. In addition, we model each qubit by a superconducting loop with three Josephson junctions, as implemented in many experiments [51–54].

By choosing the generalized flux variables ϕ_a and ϕ_b indicated in Fig. 7(a) and the phase jumps $\Delta\phi_{1,2}$ across each qubit as dynamical degrees of freedom, the Hamiltonian for this circuit can be written as (see App. B)

$$H = H_{LC} + H_{\text{int}} + H_q. \quad (22)$$

Here

$$H_{LC} = \frac{Q_a^2}{2C} + \frac{Q_b^2}{2C_b} + \frac{(\phi_a - \phi_b)^2}{2L_s} + \frac{\phi_b^2}{2L} \quad (23)$$

is the Hamiltonian for the LC resonator and

$$H_{\text{int}} = \frac{Q_b Q_q}{C_q} + \frac{\phi_q \phi_b}{L} \quad (24)$$

is the qubit-resonator coupling. In Eq. (23) and (24) the operators $Q_{a,b}$ and Q_q are the conjugate charges for the flux variables $\phi_{a,b}$ and the collective qubit flux $\phi_q = \Delta\phi_1 + \Delta\phi_2$, respectively, and $C_q = C_J(\alpha + 1/2)$ and $C_b = C_s C_q / (C_q + 2C_s)$ are the relevant capacitances. Finally, H_q is the Hamiltonian for the qubit degrees of freedom, which includes a correction term $\phi_q^2/(2L)$ from the inductive coupling. Its precise form is given in App. B, but it is not essential for following discussion.

The quadratic Hamiltonian for the electromagnetic modes can be diagonalized and written in terms of the normal mode operators c_{\pm} as $H_{LC} = \sum_{\eta=\pm} \omega_{\eta} c_{\eta}^{\dagger} c_{\eta}$. In the limit of interest, $L_s \ll L$ and $C_s \ll C$, we find that $\omega_{-} \approx 1/\sqrt{LC} = \omega_r$ and $\omega_{+} \approx 1/\sqrt{L_s C_b} \gg \omega_r$. In terms of these eigenmodes, the coupling to the qubits is given by

$$H_{\text{int}} = \sum_{\eta=\pm} i \frac{g_{Q,\eta}}{2} (c_{\eta}^{\dagger} - c_{\eta}) n_q + \frac{g_{\phi,\eta}}{2} (c_{\eta}^{\dagger} + c_{\eta}) \varphi_q. \quad (25)$$

Here we have defined the dimensionless qubit variables $\varphi_q = \phi_q/\Phi_0$ and $n_q = Q_q/(2e)$, where Φ_0 is the reduced flux quantum. In general, the inductive and capacitive couplings $g_{\phi,\pm}$ and $g_{Q,\pm}$ have a complicated dependence on all the system parameters (see App. B), but in the limit $\omega_{-} \ll \omega_{+}$ we obtain the approximate scaling for the low-frequency mode

$$\frac{g_{\phi,-}}{\omega_{-}} = \sqrt{\frac{R_Q}{\pi Z}}, \quad \frac{g_{Q,-}}{\omega_{-}} = 2 \sqrt{\frac{\pi Z}{R_Q}} \frac{C_b}{C_q} \quad (26)$$

and

$$\frac{g_{\phi,+}}{\omega_{+}} = \sqrt{\frac{R_Q}{\pi Z}} \frac{L_s}{L}, \quad \frac{g_{Q,+}}{\omega_{+}} = 2 \sqrt{\frac{\pi Z_b}{R_Q}} \frac{C_b}{C_q} \quad (27)$$

for the high-frequency mode. Here $R_Q = h/(2e)^2 \approx 6450 \Omega$ is the resistance quantum. We see that for an LC resonator with an impedance $Z = \sqrt{L/C} \approx 50 \Omega$, a

strong, primarily inductive coupling with $g_{\phi,-}/\omega_- > 1$ can be achieved. Assuming $Z_b = \sqrt{L_s/C_b} \sim Z$, the coupling to the high frequency mode is still substantial in absolute numbers, but the relevant ratio $g_{\phi,+}/\omega_+$ is suppressed by a factor L_s/L .

After introducing rescaled quadratures for the low-frequency mode, as in Eq. (4), we arrive at the rescaled Hamiltonian $\tilde{H} = H/\omega_q$, where

$$\tilde{H} = \frac{P^2}{2\mu} + \frac{X^2}{2} + \tilde{H}_q(X, P), \quad (28)$$

ω_q is the characteristic qubit frequency and $\mu = \omega_q^2/\omega_-^2$, as above. The Hamiltonian for the high-frequency dynamics,

$$\tilde{H}_q(X, P) = \tilde{\omega}_+ c_+^\dagger c_+ + \tilde{H}_{\text{int}}(X, P) + \tilde{H}_q, \quad (29)$$

now also includes the high-frequency mode and depends in general also on the momentum coordinate P due to the capacitive coupling. Note that here we do not make a two-level approximation such that $H_q(X, P)$ still contains the exact dynamics of all high-frequency degrees of freedom, which depend parametrically on the slowly varying coordinates X and P .

B. Discussion

In Table VIB we present a set of parameters for a realistic setup of two qubits, which result in $\omega_q/(2\pi) \approx 8$ GHz, $\omega_-/(2\pi) = 50$ MHz and an effective mass of $\mu \approx 2.5 \times 10^4$. The coupling parameters are $g_{\phi,-}/\omega_- \approx 7.15$ and $g_{Q,-}/\omega_- \approx 0.06$. In a pure single-mode model these values translate into a coupling parameter of $\lambda^2 \approx 0.7$, which is well above the symmetry-breaking transition in the first excited state. Note that by varying the qubit parameters by external magnetic fluxes, this coupling could also be gradually tuned across the transition [15, 21]. For the chosen values for L_s and C_s we obtain $\omega_+/(2\pi) \approx 160$ GHz, well above the qubit energy, and $g_{Q,+}/\omega_+ \approx 0.37$ and $g_{\phi,+}/\omega_+ \approx 0.01$. The value of L_s is extrapolated from the parameters reported in Ref. [55] and could even be much lower. The assumed value of C_s is within a factor of ~ 2 -3 of simulated and measured values for high-impedance coil inductors [56–58]. For these parameters we compare in Fig. 7 (b) the BO potentials obtained from the full two-mode Hamiltonian, Eq. (29), to the potential of the simplified one-mode EDM used in the previous sections. The potentials are qualitatively similar with only small shifts near $X = 0$. Note that in our simplified model, the main limitation for C_s arises from the renormalization of the qubit parameters, which partially is an artefact of modelling the distributed self- and stray capacitances of the real device in terms of a single capacitor. Leaving this aspect aside, much higher values of C_s and much lower values of ω_+ can be tolerated without substantially affecting the properties of the low-frequency mode.

Qubit	Resonator
$C_J = 2.21$ fF	$C = 79.58$ pF
$E_J/h = 336.8$ GHz	$L = 127.3$ nH
$\alpha = 0.74$	$C_s = 1.06$ fF
	$L_s = 1.27$ nH

TABLE I. The set of circuit parameters for the qubits and the LC resonator, which are used for the numerical simulations shown in Fig. 7(b).

As mentioned above, in the full model the adiabatic qubit energies obtained from Eq. (29) also depends on the momentum quadrature P . However, since this effect arises from the much smaller charge coupling and is proportional to S_y , it only induces a small second order term $\sim (g_{Q,-}/\omega_q)^2 P^2$. This correction only results in a tiny renormalization of the effective mass, which is negligible for the current set of parameters. This analysis shows that the operation of circuit QED systems in the extreme regime of ultrastrong coupling and very low frequency is experimentally feasible. Although the current model is still an oversimplification of a real device, we expect that as long as $\omega_{\text{ex}} > \omega_q$, the presence of higher excitation modes renormalizes the qubit parameters, but will not substantially change the qualitative features of the adiabatic potential curves and the measurement schemes discussed in this work.

VII. CONCLUSIONS

In summary, we have analyzed the ultrastrong coupling of multiple superconducting flux qubits to a radio-frequency electromagnetic mode. In this regime, the dynamics of the resonator mode can be modelled as an effective particle, which moves along the adiabatic potential curves generated through the coupling to the qubits. We have shown that already for a simple two-qubit setting, the first excited potential exhibits a transition from a single- to a double-well configuration. In the limit $\omega_r \rightarrow 0$ such a transition can be used as a minimal instance to study properties of quantum phase transitions, as discussed in several previous works. Importantly, characteristic signatures of this transition can be probed with regular spectroscopic measurements performed only on the qubits.

These basic findings of this work clearly demonstrate that circuit QED systems in the USC regime are not limited to tests of conventional cavity QED physics. By designing more complex potentials and measurement schemes, this adiabatic approach can be used to access a large variety of particle-like physics and wave packet phenomena with a quasi-continuum of available states. This is very different from conventional superconducting quantum circuits, where one usually only has access to a few discrete modes. While in this work we have explicitly evaluated these capabilities for a low-frequency resonator mode, an alternative strategy to access this regime could

be to work with LC resonators of only slightly below 1 GHz and push the qubit frequencies to several tens of GHz. Also in this case, values of $\mu \sim 10^3 - 10^4$ and $\lambda \gg 1$ are feasible, but different types of measurement strategies will be required.

ACKNOWLEDGMENTS

We thank Georg Arnold for valuable feedback on circuit parameters. This work was supported by the Austrian Science Fund (FWF) through Grant No. P 31701-N27 and DK CoQuS, Grant No. W 1210, and by an ESQ Discovery Grant of the Austrian Academy of Sciences (AW). J. J. García-Ripoll acknowledges support from AEI Project PGC2018-094792-B-I00, CSIC Research Platform PTI-001, and CAM/FEDER Project No. S2018/TCS-4342 (QUITEMAD-CM).

Appendix A: Adiabatic potentials

In this appendix we provide approximate analytic results for the adiabatic potentials for certain limiting cases of interest.

1. Double well transition of two qubit EDM

For two qubits we can obtain the instability point of the excited state analytically through fourth-order perturbation theory. Our starting point is the qubit Hamiltonian \tilde{H}_q given in Eq. (6). Including the bare potential $X^2/2$ for convenience it can be written as $\tilde{H}_q = \tilde{H}_0 + \tilde{H}_1$, where

$$\tilde{H}_0 = \frac{X^2}{2} + S_z + (1 + \varepsilon)\lambda^2 S_x^2, \quad (\text{A1})$$

$$\tilde{H}_1 = \sqrt{2}\lambda X S_x. \quad (\text{A2})$$

In the case of two qubits we can diagonalize \tilde{H}_0 analytically because the triplet state $|m_z = 0\rangle \equiv |T\rangle$, is decoupled from the other two states $|m_z = \pm 1\rangle \equiv |\pm 1\rangle$. The eigenenergies and eigenstates of \tilde{H}_0 are

$$\tilde{E}_T^{(0)} = \frac{X^2}{2} + \varepsilon\lambda^2, \quad |\chi_T\rangle = |T\rangle, \quad (\text{A3})$$

and

$$\tilde{E}_\pm^{(0)} = \frac{1}{2} \left(X^2 + \varepsilon\lambda^2 \pm \sqrt{4 + \varepsilon^2\lambda^4} \right), \quad (\text{A4})$$

$$|\chi_\pm\rangle = N_\pm^{-1} \left[\left(2\varepsilon^{-1}\lambda^{-2} \pm \sqrt{1 + 4\varepsilon^{-2}\lambda^{-4}} \right) |1\rangle + |-1\rangle \right]. \quad (\text{A5})$$

Here we have introduced the abbreviation $\bar{\varepsilon} = 1 + \varepsilon$ and the normalization factor $N_\pm = \sqrt{1 + (\sqrt{1 + 4\varepsilon^{-2}\lambda^{-4}} \pm 2\varepsilon^{-1}\lambda^{-2})^2}$. The singlet state

$|S\rangle$ is decoupled from the resonator and thus has the energy $\tilde{E}_S = X^2/2$, independent of λ . This leads to the splitting of the singlet and triplet states given in Eq. (14).

To obtain the instability point for the excited state $|\chi_T\rangle$ we calculate the perturbative corrections resulting from \tilde{H}_1 up to fourth order. The odd order perturbative corrections vanish since the semiclassical Hamiltonian is symmetric under the transformation $X \rightarrow -X$, $S_x \rightarrow -S_x$. Thus, the energy of $|\psi_T\rangle$ to fourth order is given by

$$\tilde{E}_T = \tilde{E}_T^{(0)} + \tilde{E}_T^{(2)} - \tilde{E}_T^{(2)} \sum_{\eta=\pm} \frac{|\langle \chi_\eta | \tilde{H}_1 | \chi_T \rangle|^2}{(\tilde{E}_T^{(0)} - \tilde{E}_\eta^{(0)})^2}, \quad (\text{A6})$$

where

$$\tilde{E}_T^{(2)} = \sum_{\eta=\pm} \frac{|\langle \chi_\eta | \tilde{H}_1 | \chi_T \rangle|^2}{\tilde{E}_T^{(0)} - \tilde{E}_\eta^{(0)}} \quad (\text{A7})$$

is the second order correction. Note that other than the last term in Eq. (A6), all other fourth-order correction terms vanish. From the zeroth-order results from above we find

$$\tilde{E}_T^{(0)} - \tilde{E}_\pm^{(0)} = \frac{1}{2} \left(\varepsilon\lambda^2 \mp \sqrt{4 + \varepsilon^2\lambda^4} \right), \quad (\text{A8})$$

$$\langle \chi_\pm | \tilde{H}_1 | \chi_T \rangle = \frac{\lambda X}{N_\pm} \left(1 + 2\varepsilon^{-1}\lambda^{-2} \pm \sqrt{1 + 4\varepsilon^{-2}\lambda^{-4}} \right). \quad (\text{A9})$$

Therefore, in total we obtain

$$\tilde{E}_T^{(2)} = -2X^2\varepsilon\lambda^4, \quad (\text{A10})$$

$$\tilde{E}_T^{(4)} = 4X^4\varepsilon\lambda^6(1 + \varepsilon^2\lambda^4), \quad (\text{A11})$$

such that

$$\tilde{E}_T = \lambda^2 + \frac{X^2}{2}(1 - 4\varepsilon\lambda^4) + 4X^4\varepsilon\lambda^6(1 + \varepsilon^2\lambda^4). \quad (\text{A12})$$

We see that \tilde{E}_T transforms from a single well to a double well when the quadratic term in X changes sign, i.e., at

$$4\varepsilon\lambda^4 = 1 \Leftrightarrow \frac{g^2}{\omega_q\omega_r} = \frac{1}{2\sqrt{1 + \varepsilon}}. \quad (\text{A13})$$

The positions of the new minima above $\lambda^2 > 1/(2\sqrt{1 + \varepsilon})$ are not predicted accurately by the above perturbative model since at the minimum the condition $\lambda X \ll 1$ is not respected anymore.

2. Structure of the ground- and first excited-state potentials for $\lambda \gg 1$

In Sec. III C we showed that in the limit $\lambda \gg 1$ the effective potentials are to a first approximation given by

$$\tilde{V}_{s,m_x}^{(0)}(X) = \frac{1}{2}(X + \sqrt{2}\lambda m_x)^2 + \varepsilon\lambda^2 m_x^2. \quad (\text{A14})$$

We calculate the effect of the free qubit Hamiltonian S_z on these potentials at the minima $X = -\sqrt{2}\lambda m_x$ and at the points where two neighbouring minima meet $X = -(1 + \varepsilon)(2m_x + 1)\lambda/\sqrt{2}$. The second order perturbative correction to the potentials is given by

$$\tilde{V}_{s,m_x}^{(2)}(X) = \sum_{m'_x \neq m_x} \frac{|\langle m'_x | S_z | m_x \rangle|^2}{\tilde{V}_{s,m_x}(X) - \tilde{V}_{s,m'_x}(X)}, \quad (\text{A15})$$

which holds for X away from the degeneracy points. At the minima $X = -\sqrt{2}\lambda m_x$ we obtain

$$\begin{aligned} \tilde{V}_{s,m_x}^{(2)}(-\sqrt{2}\lambda m_x) &= \\ \frac{-1}{4\lambda^2} \left(\frac{s_+^2(m_x)}{1 + (2m_x + 1)\varepsilon} + \frac{s_-^2(m_x)}{1 - (2m_x - 1)\varepsilon} \right) & \quad (\text{A16}) \\ \approx \frac{(1 - 3\varepsilon)m_x^2 - (1 - \varepsilon)s(s + 1)}{2\lambda^2}, \end{aligned}$$

where $s_{\pm}(m_x) = \sqrt{s(s + 1) - m_x(m_x \pm 1)}$, and to obtain the simplified expression we have assumed weak interactions $|\varepsilon(2m_x \pm 1)| \ll 1$. Thus, for weakly interacting systems the $m_x = 0$ state emerges as the ground state. Note that this semiclassical result agrees with the predictions from a strong-coupling perturbation theory of the full model for $\varepsilon = 0$ [40].

At the degeneracy points we can diagonalize the two by two matrix describing the two spin states m_x and $m_x + 1$. The reduced Hamiltonian is given by

$$\tilde{H}_{X=-\lambda(1+\varepsilon)(2m_x+1)/\sqrt{2}} = \frac{\xi}{4} \mathbf{I}_{2 \times 2} + \frac{s_+(m_x)}{2} \sigma_x, \quad (\text{A17})$$

where $\xi = \lambda^2(1 + \varepsilon) [1 + (2m_x + 1)^2\varepsilon]$ and $\mathbf{I}_{2 \times 2}$ is the 2×2 identity matrix. The eigenvalues are simply

$$\tilde{E}_{\pm} = \frac{1}{2} \left(\frac{\xi}{2} \pm s_+(m_x) \right). \quad (\text{A18})$$

Thus, the splitting between the originally degenerate states is $\tilde{\Delta}_{m_x, m_x+1} = s_+(m_x)$.

Appendix B: Two-mode circuit QED Hamiltonian

In this appendix we present additional details about the derivation of the full Hamiltonian for the circuit depicted in Fig. 7(a). We follow the standard quantization approach [59] and define the generalized flux variables

$$\phi_{a,b}(t) = \int_{-\infty}^t ds V_{a,b}(s), \quad (\text{B1})$$

where $V_{a,b}(t)$ is the voltage at the nodes indicated in Fig. 7(a). The qubits are described by the phase variables $\varphi_{1,2} = \Delta\phi_{1,2}/\Phi_0$, which represent the phase difference across the upper junction with Josephson energy αE_J . Depending on the flux qubit design, there can be additional internal dynamical degrees of freedom. For the considered three-junction design, this additional dynamical variable is the generalized flux $\phi_{-,k}$ between the two junctions in the lower arm.

The classical dynamics of this circuit is then described by the Lagrangian

$$\begin{aligned} \mathcal{L} &= \frac{C\dot{\phi}_a^2}{2} + \frac{C_s(\dot{\phi}_b - \dot{\phi}_q)^2}{2} - \frac{(\phi_a - \phi_b)^2}{2L_s} - \frac{(\phi_q - \phi_b)^2}{2L} \\ &+ \sum_k \left[\frac{C_q \Delta\dot{\phi}_k^2}{2} + \frac{C_- \dot{\phi}_{-,k}^2}{2} + \alpha E_J \cos\left(\frac{\Delta\phi_k + \Phi_e}{\Phi_0}\right) \right. \\ &\left. + 2E_J \cos\left(\frac{\Delta\phi_k}{2\Phi_0}\right) \cos\left(\frac{\phi_{-,k}}{2\Phi_0}\right) \right], \end{aligned} \quad (\text{B2})$$

where the effective capacitances are $C_q = C_J(\alpha + 1/2)$ and $C_- = C_J/2$ and $\phi_q = \sum_k \Delta\phi_k$, and Φ_e is an external magnetic flux threading the loop formed by the three junctions of the qubits. By introducing the canonical charges $Q_\eta = \partial\mathcal{L}/\partial\dot{\phi}_\eta$ for all flux variables and performing a Legendre transformation, we obtain the Hamiltonian given in Eq. (22) with

$$\begin{aligned} H_q &= \sum_k \left[\frac{Q_k^2}{2C_q} + \frac{Q_{-,k}^2}{2C_-} + \sum_l \frac{\Delta\phi_k \Delta\phi_l}{2L} \right. \\ &\left. - 2E_J \cos\left(\frac{\Delta\phi_k}{2\Phi_0}\right) \cos\left(\frac{\phi_{-,k}}{2\Phi_0}\right) - \alpha E_J \cos\left(\frac{\Delta\phi_k + \Phi_e}{\Phi_0}\right) \right]. \end{aligned} \quad (\text{B3})$$

By diagonalizing the harmonic Hamiltonian H_{LC} given in Eq. (23) we obtain the mode frequencies

$$\omega_{\pm}^2 = \frac{1}{2} \left(\omega_a^2 + \omega_b^2 \pm \sqrt{(\omega_a^2 - \omega_b^2)^2 + 4g_{ab}^2 \omega_a \omega_b} \right), \quad (\text{B4})$$

with the bare frequencies $\omega_a = 1/\sqrt{L_s C}$, $\omega_b = 1/\sqrt{L_b C_b}$ and the coupling $g_{ab} = \sqrt{Z_b/Z_a} \omega_a$. Using these normal modes, we obtain the coupling Hamiltonian H_{int} given in Eq. (25), where the couplings are

$$g_{Q,+} = 2\sqrt{\frac{\pi Z_b C_b}{R_Q C_q}} \sqrt{\frac{\omega_+}{\omega_b}} \sin(\xi) \omega_b, \quad (\text{B5})$$

$$g_{Q,-} = 2\sqrt{\frac{\pi Z_b C_b}{R_Q C_q}} \sqrt{\frac{\omega_-}{\omega_b}} \cos(\xi) \omega_b, \quad (\text{B6})$$

$$g_{\phi,+} = \sqrt{\frac{R_Q L_b}{\pi Z_b L}} \sqrt{\frac{\omega_b}{\omega_+}} \sin(\xi) \omega_b, \quad (\text{B7})$$

$$g_{\phi,-} = \sqrt{\frac{R_Q L_b}{\pi Z_b L}} \sqrt{\frac{\omega_b}{\omega_-}} \cos(\xi) \omega_b. \quad (\text{B8})$$

In these expressions the mixing angle ξ is given by

$$\tan(2\xi) = -\frac{2g_{ab}\sqrt{\omega_a\omega_b}}{\omega_a^2 - \omega_b^2}. \quad (\text{B9})$$

For $C_s, L_s \ll C, L$, respectively, we can identify ω_- as a low-frequency mode with $\omega_- \simeq \omega_r$. Using the rescaled quadratures of Eq. (4) we can write the total Hamiltonian as in Eq. (28).

- [1] A. Blais, R. S. Huang, A. Wallraff, S. M. Girvin, and R. J. Schoelkopf, Cavity quantum electrodynamics for superconducting electrical circuits: An architecture for quantum computation, *Phys. Rev. A* **69**, 062320 (2004).
- [2] A. Wallraff, D. I. Schuster, A. Blais, L. Frunzio, R.-S. Huang, J. Majer, S. Kumar, S. M. Girvin, and R. J. Schoelkopf, Strong coupling of a single photon to a superconducting qubit using circuit quantum electrodynamics, *Nature (London)* **431**, 162 (2004).
- [3] X. Gu, A. F. Kockum, A. Miranowicz, Y.-X. Liu, and F. Nori, Microwave photonics with superconducting quantum circuits, *Phys. Rep.* **718**, 1 (2017).
- [4] C. Lang, D. Bozyigit, C. Eichler, L. Steffen, J. M. Fink, A. A. Abdumalikov, Jr., M. Baur, S. Filipp, M. P. da Silva, A. Blais, and A. Wallraff, Observation of resonant photon blockade at microwave frequencies using correlation function measurements, *Phys. Rev. Lett.* **106**, 243601 (2011).
- [5] A. J. Hoffman, S. J. Srinivasan, S. Schmidt, L. Spietz, J. Aumentado, H. E. Treci, and A. A. Houck, Dispersive photon blockade in a superconducting circuit, *Phys. Rev. Lett.* **107**, 053602 (2011).
- [6] J. A. Mlynek, A. A. Abdumalikov, C. Eichler, and A. Wallraff, Observation of Dicke superradiance for two artificial atoms in a cavity with high decay rate, *Nat. Commun.* **5**, 5186 (2014).
- [7] M. H. Devoret, S. Girvin, and R. Schoelkopf, Circuit-QED: How strong can the coupling between a Josephson junction atom and a transmission line resonator be?, *Ann. Phys. (NY)* **16**, 767 (2007).
- [8] D. De Bernardis, T. Jaako, and P. Rabl, Cavity quantum electrodynamics in the non-perturbative regime, *Phys. Rev. A* **97**, 043820 (2018).
- [9] C. Ciuti, G. Bastard, and I. Carusotto, Quantum vacuum properties of the intersubband cavity polariton field, *Phys. Rev. B* **72**, 115303 (2005).
- [10] J. Casanova, G. Romero, I. Lizuain, J. J. García-Ripoll, and E. Solano, Deep Strong Coupling Regime of the Jaynes-Cummings Model, *Phys. Rev. Lett.* **105**, 263603 (2010).
- [11] P. Forn-Díaz, L. Lamata, E. Rico, J. Kono, and E. Solano, Ultrastrong coupling regimes of light-matter interaction, *Rev. Mod. Phys.* **91**, 025005 (2019).
- [12] A. F. Kockum, A. Miranowicz, S. De Liberato, S. Savasta, and F. Nori, Ultrastrong coupling between light and matter, *Nat. Rev. Phys.* **1**, 19 (2019).
- [13] P. Forn-Díaz, J. Lisenfeld, D. Marcos, J. J. García-Ripoll, E. Solano, C. J. P. M. Harmans, and J. E. Mooij, Observation of the Bloch-Siegert Shift in a Qubit-Oscillator System in the Ultrastrong Coupling Regime, *Phys. Rev. Lett.* **105**, 237001 (2010).
- [14] A. Baust, E. Hoffmann, M. Haeberlein, M. J. Schwarz, P. Eder, J. Goetz, F. Wulschner, E. Xie, L. Zhong, F. Quijandría, D. Zueco, J.-J. García Ripoll, L. Garca-Álvarez, G. Romero, E. Solano, K. G. Fedorov, E. P. Menzel, F. Deppe, A. Marx, and R. Gross, Ultrastrong coupling in two-resonator circuit QED, *Phys. Rev. B* **93**, 214501 (2016).
- [15] P. Forn-Díaz, J. J. García-Ripoll, B. Peropadre, J.-L. Orgiazzi, M. A. Yurtalan, R. Belyansky, C. M. Wilson, and A. Lupascu, Ultrastrong coupling of a single artificial atom to an electromagnetic continuum, *Nat. Phys.* **13**, 39 (2017).
- [16] F. Yoshihara, T. Fuse, S. Ashhab, Kosuke Kakuyanagi, Shiro Saito, and Kouichi Semba, Superconducting qubit-oscillator circuit beyond the ultrastrong-coupling regime, *Nat. Phys.* **13**, 44 (2017).
- [17] Z. Chen, Y. Wang, T. Li, L. Tian, Y. Qiu, K. Inomata, F. Yoshihara, S. Han, F. Nori, J. S. Tsai, and J. Q. You, Multi-photon sideband transitions in an ultrastrongly-coupled circuit quantum electrodynamics system, *Phys. Rev. A* **96**, 012325 (2017).
- [18] S. J. Bosman, M. F. Gely, V. Singh, A. Bruno, D. Bothner, and Gary A. Steele, Multi-mode ultra-strong coupling in circuit quantum electrodynamics, *Npj Quantum Inf.* **3**, 46 (2017).
- [19] P. Nataf and C. Ciuti, Protected Quantum Computation with Multiple Resonators in Ultrastrong Coupling Circuit QED, *Phys. Rev. Lett.* **107**, 190402 (2011).
- [20] G. Romero, D. Ballester, Y. M. Wang, V. Scarani and E. Solano, Ultrafast Quantum Gates in Circuit QED, *Phys. Rev. Lett.* **108**, 120501 (2012).
- [21] F. Armata, G. Calajo, T. Jaako, M. S. Kim, and P. Rabl, Harvesting Multiqubit Entanglement from Ultrastrong Interactions in Circuit Quantum Electrodynamics, *Phys. Rev. Lett.* **119**, 183602 (2017).
- [22] C. Sabin, B. Peropadre, M. del Rey, and E. Martinez-Martinez, Extracting past-future vacuum correlations using circuit QED, *Phys. Rev. Lett.* **109**, 033602 (2012).
- [23] R. Graham and M. Höhnert, Two-State System Coupled to a Boson Mode: Quantum Dynamics and Classical Approximations, *Z. Phys. B* **57**, 233 (1984).
- [24] M. D. Crisp, Application of the displaced oscillator basis in quantum optics, *Phys. Rev. A* **46**, 4138 (1992).
- [25] G. Liberti, R. L. Zaffino, F. Piperno, and F. Plastina, Entanglement of a qubit coupled to a resonator in the adiabatic regime, *Phys. Rev. A* **73**, 032346 (2006).
- [26] G. Liberti, F. Plastina, and F. Piperno, Scaling behavior of the adiabatic Dicke model, *Phys. Rev. A* **74**, 022324 (2006).
- [27] S. Ashhab and F. Nori, Qubit-oscillator systems in the ultrastrong-coupling regime and their potential for preparing nonclassical states, *Phys. Rev. A* **81**, 042311 (2010).
- [28] M. Born and R. Oppenheimer, Zur Quantentheorie der Molekeln, *Ann. Phys.* **389**, 457 (1927).
- [29] G. Johansson, L. Tornberg and C. M. Wilson, Fast quantum limited readout of a superconducting qubit using a slow oscillator, *Phys. Rev. B* **74**, 100504(R) (2006).
- [30] S. E. Nigg and M. Bittiker, Universal Detector Efficiency of a Mesoscopic Capacitor, *Phys. Rev. Lett.* **102**, 236801 (2009).
- [31] M. D. LaHay, J. Suh, P. M. Echternach, K. C. Schwab and M. L. Roukes, Nanomechanical measurement of a superconducting qubit, *Nature* **459**, 960 (2009).
- [32] J. Larson and E. K. Irish, Some remarks on ‘superradiant’ phase transitions in light-matter systems, *J. Phys. A: Math. Theor.* **50**, 174002 (2017).
- [33] I. B. Bersuker, *The Jahn-Teller Effect* (Cambridge University Press, Cambridge, 2010).
- [34] L. Bakemeier, A. Alvermann, and H. Fehske, Quantum phase transition in the Dicke model with critical and non-

- critical entanglement, *Phys. Rev. A* **85**, 043821 (2012).
- [35] S. Ashhab, Superradiance transition in a system with a single qubit and a single oscillator, *Phys. Rev. A* **87**, 013826 (2013).
- [36] M.-J. Hwang, R. Puebla, and M. B. Plenio, Quantum Phase Transition and Universal Dynamics in the Rabi Model, *Phys. Rev. Lett.* **115**, 180404 (2015).
- [37] R. Puebla, M.-J. Hwang, and M. B. Plenio, Excited-state quantum phase transition in the Rabi model, *Phys. Rev. A* **94**, 023835 (2016).
- [38] M.-J. Hwang, P. Rabl, and M. B. Plenio, Dissipative phase transition in the open quantum Rabi model, *Phys. Rev. A* **97**, 013825 (2018).
- [39] M. F. Gely, M. Kounalakis, C. Dickel, J. Dalle, R. Vatré, B. Baker, M. D. Jenkins, and G. A. Steele, Observation and stabilization of photonic Fock states in a hot radio-frequency resonator, *Science* **363**, 1072 (2019).
- [40] T. Jaako, Z.-L. Xiang, J. J. García-Ripoll, and P. Rabl, Ultrastrong coupling phenomena beyond the Dicke model, *Phys. Rev. A* **94**, 033850 (2016).
- [41] D. De Bernardis, P. Pilar, T. Jaako, S. De Liberato, and P. Rabl, Breakdown of gauge invariance in ultrastrong-coupling cavity QED, *Phys. Rev. A* **98**, 053819 (2018).
- [42] B. L. T. Plourde, J. Zhang, K. B. Whaley, F. K. Wilhelm, T. L. Robertson, T. Hime, S. Linzen, P. A. Reichardt, C.-E. Wu, and John Clarke, Entangling flux qubits with a bipolar dynamic inductance, *Phys. Rev. B* **70**, 140501(R) (2004).
- [43] Y. Todorov and C. Sirtori, Few-Electron Ultrastrong Light-Matter Coupling in a Quantum LC Circuit, *Phys. Rev. X* **4**, 041031 (2014).
- [44] M. Bamba, K. Inomata, and Y. Nakamura, Superradiant Phase Transition in a Superconducting Circuit in Thermal Equilibrium, *Phys. Rev. Lett.* **117**, 173601 (2016).
- [45] A. Garg, Tunnel splittings for one-dimensional potential wells revisited, *Am. J. Phys.* **68**, 430 (2000).
- [46] M. Vranicar and M. Robnik, Accuracy of the WKB Approximation: The Case of General Quartic Potentials, *Prog. Theor. Phys. Suppl.* **139**, 214 (2000).
- [47] R. Puebla, M.-J. Hwang, J. Casanova, and M. B. Plenio, Probing the Dynamics of a Superradiant Quantum Phase Transition with a Single Trapped Ion, *Phys. Rev. Lett.* **118**, 073001 (2017).
- [48] Note that the Kerr nonlinearity used in Ref. [39] arises directly from a quadratic shift of the transition frequency of the transmon qubit and thus has a different sign and magnitude compared to the the value of $\delta\omega_r$ derived here.
- [49] F. Yan, S. Gustavsson, A. Kamal, J. Birenbaum, A. P. Sears, D. Hover, T. J. Gudmundsen, D. Rosenberg, G. Samach, S. Weber, J. L. Yoder, T. P. Orlando, J. Clarke, A. J. Kerman, and W. D. Oliver, The flux qubit revisited to enhance coherence and reproducibility, *Nat. Commun.* **7**, 12964 (2016).
- [50] C. Caloz and T. Itoh, A Novel Composite Right-/Left-Handed Coupled-Line Directional Coupler With Arbitrary Coupling Level and Broad Bandwidth, *IEEE Trans. Microw. Theory Techn.* **52**, 980 (2004).
- [51] T. P. Orlando, J. E. Mooij, L. Tian, C. H. van der Wal, L. S. Levitov, S. Lloyd, and J. J. Mazo, Superconducting persistent-current qubit, *Phys. Rev. B* **60**, 15398 (1999).
- [52] P. Macha, G. Oelsner, J.-M. Reiner, M. Marthaler, S. André, G. Schön, U. Hübner, H.-G. Meyer, E. Ilichev, and A. V. Ustinov, Implementation of a quantum metamaterial using superconducting qubits, *Nat. Commun.* **5**, 5146 (2014).
- [53] M. J. Schwarz, J. Goetz, Z. Jiang, T. Niemczyk, F. Deppe, A. Marx, and R. Gross, Gradiometric flux qubits with a tunable gap, *New J. Phys.* **15**, 045001 (2013).
- [54] F. Deppe, M. Mariantoni, E. P. Menzel, A. Marx, S. Saito, K. Kakuyanagi, H. Tanaka, T. Meno, K. Semba, H. Takayanagi, E. Solano, and R. Gross, Two-photon probe of the JaynesCummings model and controlled symmetry breaking in circuit QED, *Nat. Phys.* **4**, 686 (2008).
- [55] L. McKenzie-Sell, J. Xie, C.-M. Lee, J. W. A. Robinson, C. Ciccarelli, and J. A. Haigh, Low-impedance superconducting microwave resonators for strong coupling to small magnetic mode volumes, *Phys. Rev. B* **99**, 140414(R) (2019).
- [56] J. M. Fink, M. Kalaei, A. Pitanti, R. Norte, L. Heinzle, M. Davanco, K. Srinivasan, and O. Painter, Quantum electromechanics on silicon nitride nanomembranes, *Nat. Commun.* **7**, 12396 (2016).
- [57] S. Barzanjeh, M. Wulf, M. Peruzzo, M. Kalaei, P. B. Dieterle, O. Painter, and J. M. Fink, Mechanical on-chip microwave circulator, *Nat. Commun.* **8**, 953 (2017).
- [58] S. Barzanjeh, E. S. Redchenko, M. Peruzzo, M. Wulf, D. P. Lewis, G. Arnold, and J. M. Fink, Stationary Entangled Radiation from Micromechanical Motion, *Nature* **570**, 480483 (2019).
- [59] U. Vool and M. Devoret, Introduction to quantum electromagnetic circuits, *Intl. J. Circuit Theor. Appl.* **45**, 897 (2016).